

Three-dimensional instability of isolated vortices

François Gallaire, Jean-Marc Chomaz

► **To cite this version:**

François Gallaire, Jean-Marc Chomaz. Three-dimensional instability of isolated vortices. *Physics of Fluids*, American Institute of Physics, 2003, 15 (8), pp.2113-2126. 10.1063/1.1580481 . hal-01024926

HAL Id: hal-01024926

<https://hal-polytechnique.archives-ouvertes.fr/hal-01024926>

Submitted on 3 Sep 2014

HAL is a multi-disciplinary open access archive for the deposit and dissemination of scientific research documents, whether they are published or not. The documents may come from teaching and research institutions in France or abroad, or from public or private research centers.

L'archive ouverte pluridisciplinaire **HAL**, est destinée au dépôt et à la diffusion de documents scientifiques de niveau recherche, publiés ou non, émanant des établissements d'enseignement et de recherche français ou étrangers, des laboratoires publics ou privés.

Three-dimensional instability of isolated vortices

F. Gallaire and J.-M. Chomaz

Citation: *Physics of Fluids* (1994-present) **15**, 2113 (2003); doi: 10.1063/1.1580481

View online: <http://dx.doi.org/10.1063/1.1580481>

View Table of Contents: <http://scitation.aip.org/content/aip/journal/pof2/15/8?ver=pdfcov>

Published by the [AIP Publishing](#)

Articles you may be interested in

[Three-dimensional swirling flows in a tall cylinder driven by a rotating endwall](#)

Phys. Fluids **24**, 014101 (2012); 10.1063/1.3673608

[Three-dimensionalization of the stratified mixing layer at high Reynolds number](#)

Phys. Fluids **23**, 111701 (2011); 10.1063/1.3651269

[Three-dimensional instabilities and transient growth of a counter-rotating vortex pair](#)

Phys. Fluids **21**, 094102 (2009); 10.1063/1.3220173

[Instability of isolated compressible entropy-stratified vortices](#)

Phys. Fluids **17**, 034102 (2005); 10.1063/1.1851451

[The three-dimensional interaction of a vortex pair with a wall](#)

Phys. Fluids **9**, 2967 (1997); 10.1063/1.869408



AIP | Journal of
Applied Physics

Journal of Applied Physics is pleased to
announce **André Anders** as its new Editor-in-Chief

Three-dimensional instability of isolated vortices

F. Gallaire and J.-M. Chomaz

Laboratoire d'Hydrodynamique (LadHyX), CNRS, École Polytechnique, 91128 Palaiseau Cedex, France

(Received 31 January 2003; accepted 17 April 2003; published 12 June 2003)

We study the three-dimensional stability of the family of vortices introduced by Carton and McWilliams [*Mesoscale/Synoptic Coherent Structures in Geophysical Turbulence*, edited by Nikhoul and Jamart (Elsevier, New York, 1989)] describing isolated vortices. For these vortices, the circulation vanishes outside their core over a distance depending on a single parameter, the steepness α . We proceed to the direct numerical simulation of the linear impulse response to obtain both temporal and spatio-temporal instability results. In the temporal instability framework, growth rates are calculated as a function of the axial wavenumber k and the azimuthal wavenumber m . The stability analysis is performed at a Reynolds number of $Re=667$. It is shown that the most unstable mode is the axisymmetric mode $m=0$, regardless of the steepness parameter in the investigated range. When the steepness α is increased the band of unstable azimuthal modes widens, i.e., larger m are destabilized. The study of the spatio-temporal spreading of the wave packet shows that the $m=2$ mode is always the fastest traveling mode, for all studied values of the steepness parameter.

© 2003 American Institute of Physics. [DOI: 10.1063/1.1580481]

I. INTRODUCTION

The structure and stability of columnar vortices have received considerable attention in the past few years since they govern geophysical flow dynamics and may also structure three-dimensional turbulent flows. In geophysical flows, the planetary rotation tends to two-dimensionalize the flow as a consequence of the Taylor–Proudman theorem. The vortices then inherit a strong vertical coherence and evolve toward columnar structures like Taylor columns. Considering only two-dimensional perturbations, Carton and McWilliams¹ showed that an axisymmetric vortex is unstable when the core is surrounded by an annulus of opposite vorticity. In that case, the vortex is said to be *isolated*, in contrast to unshielded monotonic vortices with one-signed vorticity. This pure two-dimensional instability, sometimes referred to as barotropic instability, is not the only active mechanism, for it is known since Rayleigh² that vortices with circulation decreasing away from the core are centrifugally unstable to three-dimensional axisymmetric perturbations. The scope of the present study is to determine which mechanism between azimuthal shear and centrifugal instability dominates through a fully three-dimensional instability analysis, thereby trying to answer the questions raised by Hopfinger and van Heijst³ and Orlandi and Carnevale.⁴ What are the combined effects of barotropic and centrifugal instabilities?

The rotating laboratory experiments of Kloosterziel and van Heijst,⁵ Kloosterziel and van Heijst,⁶ van Heijst, Kloosterziel, and Williams,⁷ and Carnevale and Kloosterziel⁸ have provided many interesting examples of instabilities leading to the formation of stable multipolar vortices like tripoles and quadrupoles. When these multipolar structures were not stable, they were seen to break up into pairs of dipoles. The pure 2D stability analyses of Carton and McWilliams,¹ Carnevale and Kloosterziel,⁸ and Orlandi and Carnevale,⁴ in combination with 2D numerical simulations have satisfacto-

rily reproduced the evolution and nonlinear saturation of isolated vortices into tripoles, quadrupoles, as well as their possible breakup into two dipoles. It was shown that the order of the obtained multipole was determined by the “steepness” of the base-flow profile, i.e., the typical scale of the vorticity annulus surrounding the core of the vortex, a result already demonstrated by Flierl,⁹ using piecewise constant vorticity profiles. The azimuthal shear is therefore the mechanism that leads the multipolar formation (see Chomaz, Rabaud, and Couder¹⁰).

Nevertheless, these pure two-dimensional stability analyses failed to account in essence for the observed differences between cyclones and anticyclones. It was indeed reported in the aforementioned literature that tripoles could easily be generated from cyclones but not from anticyclones which would instead preferentially break up into two dipoles. In these rotating flows Rayleigh’s criterion for centrifugal instability has to be generalized according to Kloosterziel and van Heijst⁵ through inclusion of the background rotation. Kloosterziel and van Heijst⁵ suggested further that cyclones are centrifugally stable, whereas anticyclones are centrifugally unstable, thereby “preventing in some way the flow from achieving the right conditions for tripole formation.” The use of the generalized Rayleigh’s criterion accounts for the rapid bursting of anticyclones and not of cyclones, if one follows the latter authors and admits that the centrifugal instability (due to the combined action of background rotation and the vortex’s own vorticity), when present, develops faster and stronger than the azimuthal shear instability. The present study will confirm this view, through an extension of the two-dimensional linear instability results^{1,4,8} to three-dimensional perturbations of an isolated vortex in the absence of background rotation. It is believed that the main characteristics of the centrifugal instability may be understood in the absence of background rotation. In contrast to

the work of Gent and McWilliams,¹¹ who evaluated growth rates in the f-plane quasigeostrophic limit, our study does not take into account the background rotation and should apply to vortices at high Rossby number. Smyth and McWilliams¹² recently considered the nonrotating nonstratified case in the first part of their paper but treated only one relatively smooth isolated vortex. In our study the steepness parameter will be varied from smooth isolated vortices to sharp ones.

Our study might also apply to vortex columns in homogeneous fluid as might be encountered in homogeneous turbulence.¹³ Vortex tubes, so-called “worms,” have been seen to undergo violent helical instabilities. The bursting of worms has been proposed as a strong mechanism apt to transfer energy from large scale to small scale. The most relevant model for the locally columnar vortex is not straightforward, since experimental configurations are intricate; the vortices are often neither homogeneous, nor “lonely”¹⁴ but in interaction with other vortices and with boundaries that may affect the whole dynamics through boundary effects as Eckman pumping. On the one hand, it was proposed that the bursting would be a manifestation of an instability due to external strain normal to the vortex axis (Saffman,¹⁵ Tsai and Widnall,¹⁶ or Eloy¹⁷). It was also suggested by Cadot *et al.*,¹³ on the other hand, that these worms could experience vortex breakdown as usual swirling jets with weak axial flow. In none of these experiments or numerical simulations is the presence of azimuthal shear mentioned, but in their recent model experiment concerning the bursting of vortices produced by sucking the boundary layer of a channel flow, Bottausci and Petitjean¹⁸ measure a radially decreasing circulation pointing to an isolated vortex. Since this flow is highly nonhomogeneous, its dynamics will be controlled not only by the local temporal instability but also affected by the way perturbations propagate along the vortex axis.

A spatio-temporal study is therefore performed as in Delbende *et al.*¹⁹ in order to determine the fastest and slowest propagating modes. The spatio-temporal selected modes are relevant in experiments where perturbations are localized due to the interaction with another coherent structure in turbulence or due to the inlet condition if the flow is open (Huerre and Rossi²⁰). By contrast, if perturbations are homogeneous in space, the dynamics is governed by the temporal instability. The paper, which is restricted to the study of a single columnar vortex with decreasing circulation outside the core, is organized as follows. The one-parameter family of isolated vortices introduced by Carton and McWilliams¹ used as basic flow is defined in Sec. II together with the identification of the physical mechanisms for instability and associated classical stability criteria. The numerical method and the diagnostic tools are outlined in Sec. III. In Sec. IV, temporal stability results are presented, whereas the spatio-temporal evolution of the wave packet is described in Sec. V. A more detailed study of the wave packet is postponed to Sec. VI, before the main results are summarized and discussed in the final section (Sec. VII).

II. BASE FLOW AND PHYSICAL INSTABILITY MECHANISMS

The description of monopolar vortices is made easier through the introduction of a polar coordinate system $\mathbf{r}=(x, r, \theta)$, with the x axis parallel to the rotation axis. The corresponding velocity components \mathbf{u} are denoted accordingly (u_x, u_r, u_θ) . The vortex consists of a purely azimuthal flow about the x axis and is supposed to be spatially invariant in the x direction so that the velocity field can be written $\mathbf{u}=(0, 0, u_\theta(r))$. We use the family of profiles introduced by Carton and McWilliams¹ defined by the steepness parameter α

$$u_\theta^+ = U \frac{r^+}{R} \exp(-(r^+/R)^\alpha), \quad (1)$$

where the symbol $+$ denotes dimensional quantities, R and U are characteristic length and velocity scales, serving to form the Reynolds number

$$\text{Re} = \frac{UR}{\nu}, \quad (2)$$

where ν is the kinematic viscosity. Introducing the dimensionless variables $r=r^+/R$ and $u_\theta=u_\theta^+/U$, the base flow becomes

$$u_\theta = r e^{-r^\alpha}. \quad (3)$$

Whatever the positive value of α considered, these vortices are fully screened since the circulation vanishes at infinity. In the case $\alpha=2$ it is called a Gaussian vortex. The stability of the Gaussian vortex was first studied on the f-plane by Gent and McWilliams¹¹ and more recently by Smyth and McWilliams.¹² Flor and van Heijst²¹ have shown that it fits their experimental vortices.

Azimuthal velocity profiles are plotted for different parameter values α in Fig. 1(a). The maximal azimuthal velocity u_θ^{max} increases with α together with its radial location r^{max} . As seen in Fig. 1(b), which displays the corresponding axial vorticity $\omega_x=(r^{-1}d(ru_\theta)/dr)$, the annulus of opposite vorticity narrows and intensifies as α is increased and it can be shown that its amplitude is asymptotically proportional to α .

A precise examination of both the azimuthal velocity and the axial vorticity profiles allows us to determine the stability of a vortex depending on the axial and azimuthal wavenumber k and m from well-known criteria. Let us review them briefly.

- (i) The two-dimensional ($k=0$) inflectional Rayleigh theorem for *azimuthal shear* states that a necessary condition for the axisymmetric flow to be unstable to azimuthal Kelvin–Helmholtz shear waves is

$$\frac{d\omega_x}{dr} = 0. \quad (4)$$

The corresponding point is depicted by a full circle in the case $\alpha=4$ in Fig. 1(b). This criterion is the generalization of Rayleigh’s inflection point theorem to cir-

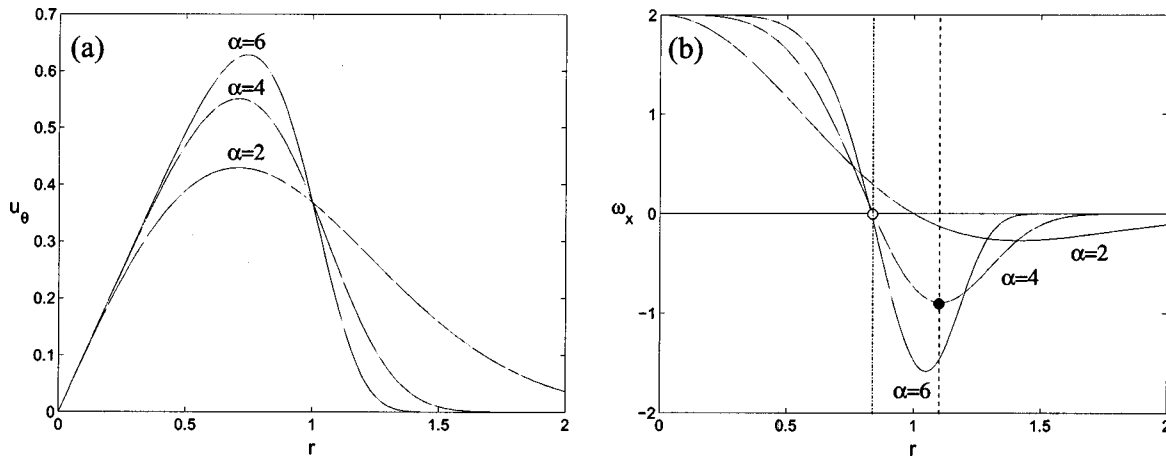


FIG. 1. (a) Dimensionless azimuthal velocity profiles $u_\theta(r)$ for various $\alpha=2, 4,$ and 6 ; (b) dimensionless axial vorticity profiles $\omega_x(r)$ for the same values of α . For $\alpha=4$, the filled circle corresponds to the locus of a minimum in axial vorticity signaling an eventual azimuthal shear instability and the open circle corresponds to the radius where the axial vorticity becomes negative and Rayleigh's criterion applies.

cular geometry.²² The physical mechanism underlying this instability is the well-known Kelvin–Helmholtz mechanism.

- (ii) The axisymmetric ($m=0$) Rayleigh² centrifugal criterion states that a sufficient and necessary (as demonstrated by Synge²³) condition for axisymmetric instability is that the square of the circulation be decreasing

$$\frac{d}{dr}(ru_\theta)^2 < 0, \tag{5}$$

which is equivalent to

$$u_\theta \omega_x < 0, \tag{6}$$

where ω_x is the axial vorticity. The physical origin of the centrifugal instability is an unstable stratification in angular momentum. The corresponding point to the right of which the flow is centrifugally unstable is depicted by a hollow circle in the case $\alpha=4$ in Fig. 1(b).

- (iii) Finally, the sufficient condition of Leibovich and Stewartson²⁴ and the necessary condition of Ludwig²⁵ for helical perturbations ($m \neq 0, k \neq 0$ in general) to be unstable, both applying in general to vortices with axial flow, extrapolate as

$$u_\theta \frac{d}{dr}(ru_\theta) < 0. \tag{7}$$

This condition is identical to the Rayleigh centrifugal criterion (5), which therefore finally represents a necessary and sufficient condition for helical as well as axisymmetric instability.

These four inviscid criteria are fulfilled by the base flow for all positive values of α . Therefore, when viscosity is neglected, the vortices considered in the present paper are unstable with respect to axisymmetric ($m=0$) centrifugal modes and fully three-dimensional, helical ($m \neq 0$ and/or $k \neq 0$) centrifugal and shear modes, and possibly also to two-dimensional ($k=0, m \neq 0$) shear modes. However, none of

these criteria predicts which mode will dominate: our aim is precisely to understand the temporally and spatio-temporally selected wavenumber pairs (k, m) . Previous studies of this model (except Smyth and McWilliams in the case $\alpha=2$) are restricted to the two-dimensional case, ($k=0$). Figure 2 illustrates the structure of some instabilities with various wavenumbers k and m . The vortex rotates in the direct sense according to the orientation of the x axis and the right-hand rule. The structure in (a) is an axisymmetric instability like in Taylor–Couette flow, the azimuthal deformation in (b) corresponds to a two-dimensional instability, whereas the helical structure depicted in (c) is an $m=2$ positive helical mode. The sense of winding of a helix will be said to be positive (respectively, negative) when the product $k \times m$ is positive (respectively, negative). For a positive helical mode, the helix is screwed in such a way that when traveling up in the positive x direction, the helix winds itself in the clockwise direction, i.e., in the negative sense of rotation.

III. GOVERNING EQUATIONS AND NUMERICAL METHOD

This section outlines the numerical method used to obtain both the temporal instability curves and the spatio-temporal results concerning the evolution of the wave packet through a single simulation.

One first expands the perturbation into normal form $e^{i(kx+m\theta-\omega_m t)}$, where the axial and azimuthal wavenumbers k and m are assumed to be real, whereas the frequency is complex $\omega_m = \omega_{m,r} + i\omega_{m,i}$. For each wavenumber pair (k, m) , the temporal stability study of the flow consists of determining the selected pulsation $\omega_{m,r}$ and growth rate $\omega_{m,i}$ at a given Reynolds number. This determination of the dispersion relation is usually done by solving the Orr–Sommerfeld equation. In complement to this so-called temporal instability study, the analysis of the impulse response, through the examination of the spreading of the wave packet, constitutes the so-called spatio-temporal stability analysis, leading to the distinction between absolute and convective instabilities²⁰ when one is dealing with open flows. The usual

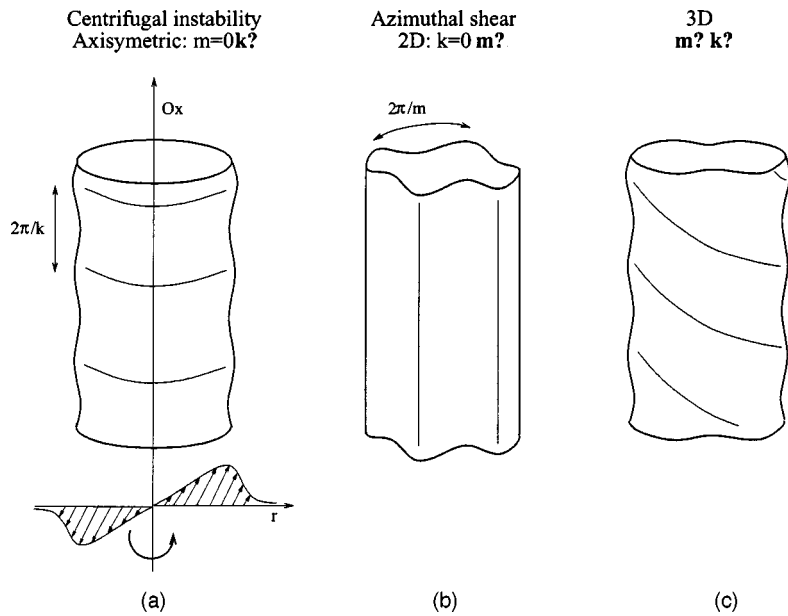


FIG. 2. Different types of instabilities: (a) axisymmetric centrifugal instability ($m=0$, $k=1$); (b) azimuthal two-dimensional instability ($m=4$, $k=0$); (c) full three-dimensional instability ($m=+2$, $k=1$); note that, according to the orientation of the x axis in (a), the helical mode considered in (c) is a positive helical mode.

way to determine the impulse response with help of the Orr–Sommerfeld equation goes through the exhaustive tracking procedure of saddle points between adequate spatial branches.

The strategy adopted in this paper is to perform a direct numerical simulation of the linearized impulse response of the vortex. This method was introduced by Brancher and Chomaz²⁶ and applied by Delbende *et al.*¹⁹ to compute the instabilities of the Batchelor vortex. The main characteristic of the method is that it gives access only to the most amplified mode, but the use of the symmetries of the problem (here, the azimuthal Fourier decomposition) considerably increases the amount of retrieved informations. Furthermore, to extract more modes, Krylov methods as those used recently by Edwards *et al.*²⁷ or Julien *et al.*²⁸ may allow one to recover as many leading amplified modes as one wishes. In the present study the leading mode will provide enough information and the sophistication of the Krylov method is not compulsory.

A. Numerical implementation

We consider the evolution of infinitesimal disturbances superimposed on the basic flow profiles and governed by the linearized incompressible Navier–Stokes equations. The viscous diffusion term acting on the basic flow has been neglected. The Reynolds number as defined in (2) is $\text{Re}=667$.

We use the code described by Brancher and Chomaz²⁶ and Delbende *et al.*,¹⁹ adapted from the original code of Vincent and Meneguzzi.²⁹ The linearized Navier–Stokes equations are projected onto $720 \times 128 \times 128$ Fourier modes along three Cartesian directions (Ox is along the axis of the vortex, Oy and Oz are two perpendicular arbitrary directions). In physical space, this corresponds to a parallelepipedic mesh with resolution $dy=dz=0.05$ and $dx=0.1$ in a domain of lengths $Ly=Lz=6.4$ and $Lx=72$. Fine resolutions in the y - and z directions are necessary owing to the small scales induced by the intensity of the shear layer which increases with

α . Such a resolution has become possible recently thanks to the NEC SX5 at IDRIS. We explored the range of steepness parameter from $\alpha=1$ to $\alpha=8$. $Ly=Lz$ are chosen large enough so that the confinement due to the periodicity in y and z is weak. Transformed into the Fourier space, the large size of the box in the axial direction, Lx , guarantees a high resolution dk for the axial wavenumber k , whereas the fine resolution dx gives a large cutoff wavenumber k_c . These resolutions have been found to be sufficient to characterize both the temporal and the spatio-temporal instabilities of the flow properly. In particular, the convergence has been checked by performing a simulation with resolution $1440 \times 196 \times 196$, and $dy=dz=0.033$ and $dx=0.05$ in the steepest case $\alpha=8$ and by checking that all the quantities reported in the following vary by less than 5% in the worst case. The time step is chosen in order to verify a CFL-type numerical stability condition, $dt=0.01$ when $dx=0.1$.

In order to mimic a delta-function forcing in space and time, the initial conditions are chosen as in Delbende *et al.*¹⁹ and satisfactorily represent a divergence-free localized impulse of characteristic velocity perturbation amplitude 0.1 contained within a sphere of radius 0.5 and located at $x_0=Lx/2$ (the middle of the box), $r_0=1$ and $\theta=15^\circ$ in order to feed energy initially to all azimuthal wavenumbers. It should be noticed that the size of the initial impulse is a tradeoff between having a compact perturbation yielding a well-defined localization and therefore a good approximation of a Dirac function and a large, smooth enough perturbation so as to avoid the Gibbs phenomenon arising from the truncation in the Fourier space and to keep initial perturbations strictly equal to the computer round-off away from the impulse location.

At a given time, the integration of the linearized Navier–Stokes equations provides us with the full velocity and vorticity field associated with the evolution of the wave packet. We choose to characterize the wave packet solely by the perturbation in the axial velocity, and define

$$a(x, y, z, t) \equiv u_x(x, y, z, t).$$

Such an assumption gives access to the asymptotic temporal and spatio-temporal growth rate but restricts access only to the axial velocity component of the eigenfunctions. The use of the three components of the velocity field is possible and does not affect the procedure, but the gain is limited to the knowledge of the two extra eigenfunctions in azimuthal and radial velocity and is not worth the CPU consumption. The amplitude a is transformed through a change of coordinate system into $a(x, r, \theta, t)$, where the cylindrical grid has 40 points in the radial direction between $r=0$ and $r=R_{\max}=Ly(=Lz)$ and 32 points in the azimuthal direction. This restricts, therefore, the analyzed azimuthal wavenumber range to $|m| < 16$, but we have systematically checked that no aliasing errors are introduced by this cutoff since in all simulations, modes with $|m| > 16$ were always found to be stable.

B. Temporal instabilities

Since the spectrum of the initial perturbation is broad, all the azimuthal and axial wavenumbers are initially excited. The temporal evolution of each individual azimuthal and axial wavenumber may be followed through an axial and azimuthal double-Fourier transform that leads from $a(x, r, \theta, t)$ to $\hat{a}(k, r, m, t)$. This complex signal is integrated between $r=0$ and $r=R_{\max}$

$$\hat{A}_m(k, t) = \left(\int_0^{R_{\max}} |\hat{a}(k, r, m, t)|^2 r dr \right)^{1/2}. \tag{8}$$

The temporal growth rate between t_1 and t_2 is then given by

$$\hat{\omega}_{m,i}(k, t_1, t_2) \equiv \frac{\ln(\hat{A}_m(k, t_2)/\hat{A}_m(k, t_1))}{t_2 - t_1}. \tag{9}$$

When t_1 and t_2 are large enough, the evolution of the flow is dominated for each k and m by a single mode (the most unstable mode) growing exponentially. Thus

$$\lim_{t_1, t_2 \rightarrow \infty} \hat{\omega}_{m,i}(k, t_1, t_2) = \hat{\omega}_{m,i}(k), \tag{10}$$

where $\hat{\omega}_{m,i}(k)$ is the growth rate of the leading eigenmode.

As noticed by Delbende *et al.*,¹⁹ the time increment $t_2 - t_1$ has to be large enough in order to circumvent low-frequency oscillations due to mode interaction. In our calculations $t_2 = 2 \times t_1$ and t_1 is chosen in order for $\hat{A}_m(k, t_1)$ and $\hat{A}_m(k, t_2)$ to be both at least three orders of magnitudes larger than the initial amplitude $\hat{A}_m(k, t=0)$. This is done in order to avoid spurious growth rates due to round-off errors of the Fourier transforms. This also guarantees that the transient regime has been left. In addition we check that $\hat{\omega}_{m,i}(k, t_1, 1.5 \times t_1)$, $\hat{\omega}_{m,i}(k, t_1, 2 \times t_1)$, and $\hat{\omega}_{m,i}(k, 1.5 \times t_1, 2 \times t_1)$ are closer than 1% in order to ensure convergence. When these conditions are not met, we consider that our method fails in determining $\hat{\omega}_{m,i}(k)$. This will be seen in the next section to be the case only for $m=1$ at small k .

The associated phase $\hat{\phi}_m(k, t)$ is measured at the location r_0 of the radial impulse

$$\hat{\phi}_m(k, t) = \arg(\hat{a}(k, r_0, m, t)), \quad \text{with } 0 \leq \hat{\phi}_m(k, t) < 2\pi. \tag{11}$$

The real part of the pulsation is given by

$$\hat{\omega}_{m,r}(k) \sim - \frac{\hat{\phi}_m(k, t_3) - \hat{\phi}_m(k, t_2)}{t_3 - t_2}, \tag{12}$$

as soon as t_3 and t_2 are sufficiently large to quit the transient regime. As explained in Delbende *et al.*,¹⁹ the time interval $t_3 - t_2$ is selected to be short enough to circumvent the difficulties due to the discontinuous nature of the phase function $\hat{\phi}_m(k, t)$ whenever it reaches 0 or 2π .

It is important to note that the real nature of the considered signal $a(x, r, \theta, t)$ induces strong symmetries. Denoting by $\hat{\omega}_m(k)$ the complex pulsation, the following symmetry holds:

$$\hat{\omega}_{-m}(-k) = -\hat{\omega}_{+m}^*(k). \tag{13}$$

In other words, there are only *two* and not four different perturbations of wavenumbers $|k|$ and $|m|$ in absolute value, singled out by the sign of the product $k \times m$. We recover the difference between positive and negative helical modes as discussed in Sec. II. This demonstrates that it is sufficient to describe the temporal instabilities in half of the parameter space $k-m$. Our choice, which is a common one in the literature, is to prescribe $k \geq 0$ and let m be a signed quantity. Within that convention, since the sense of winding is given by the sign of the product $m \times k$, modes with positive m will be effectively positive helical modes [like the one in Fig. 2(c)], whereas modes with negative m will effectively correspond to negative helical modes.

C. Spatio-temporal instabilities

In the spatio-temporal formulation, we consider the development of the wave packet along rays of given velocity $x/t = v_g$. In order to define the amplitude of the wave packet unambiguously, it is convenient, as in Huerre and Monkewitz³⁰ or Delbende *et al.*,¹⁹ to introduce the analytical complex field variable

$$\bar{a}(x, r, m, t) = \left[\delta(x) + \frac{i}{\pi x} \right] * \tilde{a}(x, r, m, t), \tag{14}$$

where $\tilde{a}(x, r, m, t)$ is the azimuthal Fourier transform of $a(x, r, \theta, t)$, δ is the Dirac function, and the symbol $*$ designates the convolution operator with respect to x . This convolution is processed in spectral space through the so-called Hilbert transform

$$\hat{\tilde{a}}(k, r, m, t) = 2H(k)\hat{a}(k, r, m, t), \tag{15}$$

where $H(k)$ denotes the Heaviside function. In other words, the Fourier transform of the analytical field is obtained by setting to zero all the Fourier modes of negative streamwise wavenumber. The analytical field $\bar{a}(x, r, m, t)$ is then obtained by an inverse axial Fourier transform from $\hat{\tilde{a}}(k, r, m, t)$. The cancellation of the negative k plane is a consistent choice with the convention to consider k positive

and m signed in temporal theory instability theory as outlined above. In particular, positive helical modes correspond to $m > 0$ and negative helical modes to $m < 0$.

As in the temporal analysis, the integration of the analytical field $\bar{a}(x, r, m, t)$ yields the amplitude \bar{A} defined by

$$\bar{A}_m(x, t) = \left(\int_0^{R_{\max}} |\bar{a}(x, r, m, t)|^2 r dr \right)^{1/2}. \quad (16)$$

According to steepest-descent arguments,³¹ the long-time behavior of the wave packet along each spatio-temporal ray $x/t = v_g$ is

$$\bar{A}_m(x, t) \propto t^{-1/2} e^{(\bar{k}_m(v_g)(x-x_0) - \bar{\omega}_m(v_g)t)} \quad t \rightarrow \infty, \quad (17)$$

where $\bar{k}_m(v_g)$ and $\bar{\omega}_m(v_g)$ represent the complex wavenumber and frequency traveling at the group velocity v_g , respectively. In (17), the real part of the exponential

$$\bar{\sigma}_m(v_g) = \bar{\omega}_{m,i}(v_g) - v_g \times \bar{k}_{m,i}(v_g), \quad (18)$$

denotes the temporal growth rate observed while traveling at the group velocity v_g , and it can be evaluated for large t directly from (17) as

$$\bar{\sigma}_m(v_g) \propto \frac{\partial}{\partial t} \ln(t^{1/2} \bar{A}_m(v_g t + x_0, t)). \quad (19)$$

As done previously in Eqs. (9)–(10), Eq. (19) is temporally discretized into

$$\bar{\sigma}_m(v_g, t_1, t_2) \equiv \frac{\ln(\bar{A}_m(v_g t_2 + x_0, t_2) / \bar{A}_m(v_g t_1 + x_0, t_1))}{t_2 - t_1} + \frac{\ln(t_2 - t_1)}{2(t_2 - t_1)}. \quad (20)$$

The instants t_1 and t_2 are chosen in the same manner as for the determination of temporal growth rates. The associated phase distribution is measured at the radial location r_0

$$\bar{\phi}_m(x, t) = \arg(\bar{a}(x, r_0, m, t)), \quad \text{with } 0 \leq \bar{\phi}_m(k, t) < 2\pi, \quad (21)$$

and allows us to retrieve the real parts of the complex wavenumber and pulsation, $\bar{k}_{m,r}(v_g)$ and $\bar{\omega}_{m,r}(v_g)$, according to

$$\bar{k}_{m,r}(v_g) \sim \frac{\bar{\phi}_m(v_g t_2 + x_0 + \delta x, t_2) - \bar{\phi}_m(v_g t_2 + x_0, t_2)}{\delta x}, \quad (22)$$

and

$$\bar{\omega}_{m,r}(v_g) \sim - \frac{\bar{\phi}_m(v_g t_2 + x_0, t_3) - \bar{\phi}_m(v_g t_2 + x_0, t_2)}{t_3 - t_2}. \quad (23)$$

Frequencies are evaluated over time increments shorter than the period of the oscillation. Note finally that $\bar{\omega}_{m,i}(v_g)$ as well as $\bar{k}_{m,i}(v_g)$ might also be computed if necessary.¹⁹

Unfortunately, as already noticed by Delbende *et al.*,¹⁹ according to signal processing theory, Hilbert transforms degrade the wave packet's localization considerably when the corresponding spectrum does not vanish at $k = 0$. This results in the appearance of "tails" which apodize the wave packet

outside of its main peak! In such cases, tails of the wave packet that determine the spreading velocity of the modes will still be accessible, but with less precision, by making use of the azimuthal Fourier transform $\tilde{a}(x, r, m, t)$ of the signal $a(x, r, \theta, t)$ in place of the associated analytical signal $\bar{a}(x, r, m, t)$ in steps (16) to (21) with the symbol \sim replacing the symbol $\bar{\cdot}$ on all quantities of interest.

This choice has strong implications since the demodulation is not done and all above-defined quantities will keep oscillating in time and space due to the phase variations. It also must be understood that in cases where the Hilbert transform cannot be used and the Fourier transform is used instead, positive and negative helical modes cannot be separated and the one with the largest growth rate will dominate. This can be seen for instance in the fact that, due to the real nature of $a(x, r, \theta, t)$

$$\tilde{a}(x, r, m, t) = \tilde{a}^*(x, r, -m, t), \quad (24)$$

where the symbol $*$ denotes the complex conjugate. This implies the following relations:

$$\tilde{A}_{-m}(v_g) = \tilde{A}_{+m}(v_g), \quad (25a)$$

$$\tilde{\sigma}_{-m}(v_g) = \tilde{\sigma}_{+m}(v_g), \quad (25b)$$

$$\tilde{k}_{-m,r}(v_g) = -\tilde{k}_{+m,r}(v_g), \quad (25c)$$

$$\tilde{\omega}_{-m,r}(v_g) = -\tilde{\omega}_{+m,r}(v_g). \quad (25d)$$

Equation (25b) demonstrates that, within the framework of Fourier transforms, there is no distinction between the growth rate of a $+m$ mode and of its opposite $-m$. This allows us to define an overall growth rate $\tilde{\sigma}_{|m|}$

$$\tilde{\sigma}_{|m|}(v_g) \stackrel{\text{def}}{=} \tilde{\sigma}_{+m}(v_g), \quad (26)$$

pertaining to both modes of helical order $|m|$ and opposite winding directions. As a consequence, when Fourier transforms are used there is a strong contrast with the convention adopted previously in temporal stability theory or when Hilbert transforms are used: the sign of the winding of a helical mode on a given ray $x/t = v_g$ is not given by the sign of m but by the sign of the product, $m \times \tilde{k}_{m,r}$. One can easily verify that Eq. (24) implies that $\tilde{k}_{-m,r}(v_g) = -\tilde{k}_{m,r}(v_g)$, so that $m \times \tilde{k}_{m,r} = -m \times \tilde{k}_{-m,r}$.

D. Symmetry considerations

Since there is no advection in the streamwise direction, the problem is invariant under the transformation

$$(x, m, k, \omega) \leftrightarrow (-x, m, -k, \omega), \quad (27)$$

or by virtue of the real nature of the signal $a(x, r, \theta, t)$ [see Eq. (13)], to

$$(x, m, k, \omega) \leftrightarrow (-x, -m, k^*, -\omega^*), \quad (28)$$

where the symbol $*$ denotes the complex conjugate. When k is real, as in the temporal stability framework, this leads to

$$\hat{\omega}_{-m}(k) = -\hat{\omega}_{+m}^*(k). \quad (29)$$

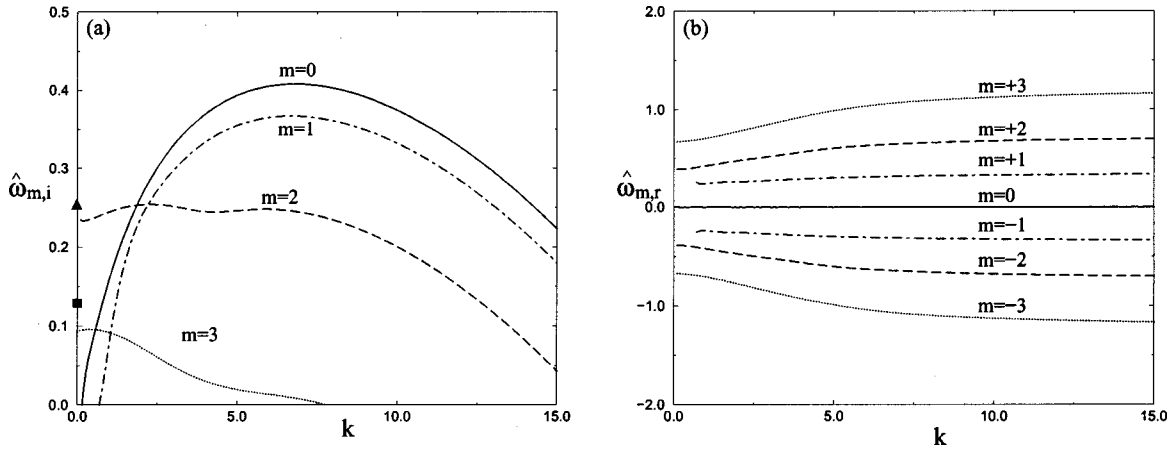


FIG. 3. (a) Temporal growth rate $\hat{\omega}_{m,i}(k)$ as a function of the axial wavenumber k for $\alpha=4$ and various values of m [$m=0$ (full line), $m=\pm 1$ (dotted-dashed), $m=\pm 2$ (dashed) and $m=\pm 3$ (dotted)]; full symbols on the $k=0$ axis correspond to the results of Carnevale and Kloosterziel (Ref. 8) for $m=2$ (triangle) and $m=3$ (square). (b) Angular frequency $\hat{\omega}_{m,r}(k)$ as a function of k for the same settings.

In terms of spatio-temporal quantities, when the analytical signal is considered, one is led to the following symmetries:

$$\bar{A}_{-m}(-v_g) = \bar{A}_{+m}(+v_g), \quad (30a)$$

$$\bar{\sigma}_{-m}(-v_g) = \bar{\sigma}_{+m}(+v_g), \quad (30b)$$

$$\bar{k}_{-m,r}(-v_g) = \bar{k}_{+m,r}(+v_g), \quad (30c)$$

$$\bar{\omega}_{-m,r}(-v_g) = -\bar{\omega}_{+m,r}(+v_g). \quad (30d)$$

When the properties of the wave packet are evaluated by means of the Fourier transforms, and the trivial symmetries (25) are also invoked, one ends up with the following relations:

$$\tilde{A}_m(-v_g) = \tilde{A}_m(+v_g), \quad (31a)$$

$$\tilde{\sigma}_m(-v_g) = \tilde{\sigma}_m(+v_g), \quad (31b)$$

$$\tilde{k}_{m,r}(-v_g) = -\tilde{k}_{m,r}(+v_g), \quad (31c)$$

$$\tilde{\omega}_{m,r}(-v_g) = \tilde{\omega}_{m,r}(+v_g). \quad (31d)$$

IV. TEMPORAL INSTABILITY

This section deals with temporal instability. As specified above, k is taken positive without loss of generality. In Fig. 3, the growth rate $\hat{\omega}_{m,i}(k)$ obtained by formula (9) is plotted as a function of the axial wavenumber k for different values of the azimuthal wavenumber m and for a steepness parameter $\alpha=4$.

Since $\hat{\omega}_{-m,i}(k) = \hat{\omega}_{+m,i}(k)$ [see Eq. (29)], only positive m are reported. In the two-dimensional limit ($k=0$), it is seen that the only unstable modes for $\alpha=4$ are $m=2$ and $m=3$, $m=4$ and larger (not shown) being stable. As suggested by Flierl,⁹ this shows the existence of a cutoff wavenumber m_α , above which all wavenumbers are entirely stabilized at $k=0$. For direct comparison, the inviscid results obtained by Carton and McWilliams,¹ Carnevale and Kloosterziel,⁸ and Orlandi and Carnevale⁴ are represented in Fig. 3(a) by full symbols. Our growth rates are slightly smaller than their inviscid growth rates because of the viscosity. In the 2D case, Orlandi and Carnevale⁴ have also

demonstrated that the vortex is unstable only above the threshold steepness parameter of $\alpha=1.85$. Even if condition (4) is fulfilled as soon as $\alpha \geq 0$, the threshold value of $\alpha_c = 1.85$ is consistent with (4) since it is only a necessary condition for 2D instability. We have observed that the vortex is stable at $k=0$ when $\alpha=1$ and unstable when $\alpha=2$, in agreement with the inviscid instability threshold $\alpha_c = 1.85$, even in the presence of viscous effects.

For $\alpha=4$, when k increases, $m=0$ and $m=1$ modes become unstable and reach a maximum growth rate at $k_0 \sim 6.8$ and $k_1 \sim 6.7$. By contrast, the growth rate of the $m=3$ mode continuously decreases with increasing k . The nature of mode $m=2$ is more complex, the curve of Fig. 3 presenting two local maxima at $k \sim 2.3$ and $k \sim 5.5$. For $k \geq 2$, the most unstable mode becomes $m=0$. It is noteworthy to remark that for all m , the axial wavenumbers k larger than a cutoff wavenumber k_m^c are quenched, in contrast with the results reported by Smyth and McWilliams¹² for the modes $m=0, 1$, and 2 and $\alpha=2$ when the flow is inviscid. In that case, the growth rate asymptotes to a finite value when k goes to infinity. In our study, this behavior is not observed because of the stabilizing effect of viscosity at large k .

Figure 3(b) displays the frequency $\hat{\omega}_{m,r}$ of the instability waves as a function of k . First, note that the $m=0$ mode is stationary, as imposed by symmetry (29). The absolute value of the frequency of the modes increases with m , and it can be shown that the phase velocity ω_r/m only weakly depends on m . Positive helical modes ($m>0$) have positive frequencies and negative helical modes ($m<0$) have negative frequencies, so that, in a transverse plane, at a given x station, both rotate in time in the same direction as the vortex, since $\hat{\omega}_{m,r} \times m$ is positive. This symmetry between positive and negative m results from (29). The fact that both positive and negative helical modes rotate at the same speed and in the same direction as the vortex is in agreement with the results of Smyth and McWilliams¹² for a Gaussian ($\alpha=2$) vortex (note that the vorticity is taken negative in the core of the vortex in their study, whereas the core vorticity is positive herein).

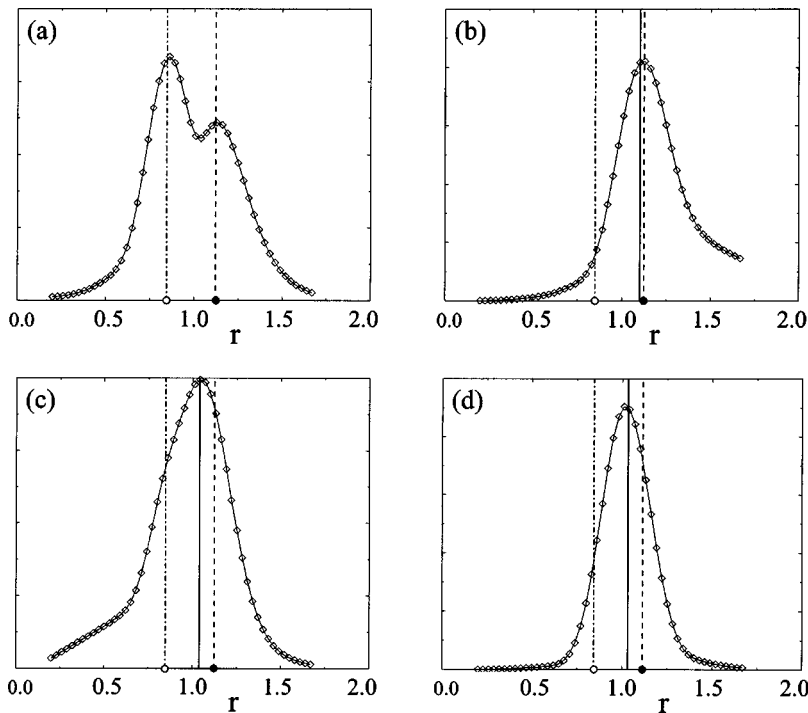


FIG. 4. (a) Eigenfunction at $k=6.8, m=0$; (b) eigenfunction at $k=0, m=2$; (c) eigenfunction at $k=6.7, m=1$; (d) eigenfunction at $k=5.5, m=2; \alpha=4$; the ordinate scale is arbitrary; the vertical line represents the critical radius r_c ; the dashed line with full circle represents the radius of minimum axial vorticity and the dotted-dashed line with hollow circle the radius above which the Rayleigh criterion for centrifugal instability is verified.

In the case $\alpha=4$, in complement to Fig. 3, Fig. 4 displays the axial velocity profile of four eigenfunctions associated with four different relevant wavenumber pairs. Figure 4(a) depicts the eigenfunction for the axisymmetric mode ($m=0$) for $k_0^{\max}=6.7$, where the growth rate is maximum, which shows two peaks. The axisymmetric mode ($m=0$) is only sensitive to the centrifugal instability, which sets in when Rayleigh’s criterion (5) is valid, i.e., to the right dashed-dotted line in Fig. 4(a) [the hollow circle in Fig. 1(b) and Fig. 4(a)]. Figure 4(a) shows that the eigenfunction presents a peak in the vicinity of the radius where the Rayleigh criterion first applies and vanishes close to the vortex center where the flow is centrifugally stable. A second peak is observed where $d\omega_x/dr=0$. Figure 4(b) depicts the eigenfunction related to a pure 2D mode with $k=0$ and $m=2$. This type of instability is known to be entirely due to azimuthal shear via the Kelvin–Helmholtz mechanism. Note that the peak is now located in the vicinity of the point where $d\omega_x/dr=0$, i.e., the point designated by a dashed vertical line and a full circle [see also Fig. 1(b)].

This peak is also close to the critical radius r_c marked by a solid vertical line and defined for $m \neq 0$ such that the azimuthal phase velocity is equal to the angular velocity of the basic flow

$$\frac{\omega_{r,m}}{m} = \frac{U_\theta(r_c)}{r_c}. \tag{32}$$

This is consistent with the results of Smyth and McWilliams,¹² who have noticed a strong link between the critical radius and the location of the maximum of the eigenfunction, in the case $\alpha=2$. Figures 4(c) and (d) depict eigenfunctions of helical instabilities, respectively, the $m=1$ bending mode at its most unstable wavenumber $k_1^{\max}=6.7$ and the $m=2$ mode for $k_2^{\max}=5.5$. The eigenfunctions are

seen to be peaked in the region of shear denoted by the dashed vertical line, remarkably correlated to the location of the critical radius [Eq. (32)].

Let us briefly consider the effects of the Reynolds number in the case of $\alpha=5$ by considering in addition to $Re=667$ also $Re=333$ and $Re=1333$. Results are displayed in Fig. 5 for the mode $m=2$. We observe that the cutoff wavenumber k_2^c increases with the Reynolds number like the maximal growth rate $\hat{\omega}_{2,i}^{\max}$, the two-dimensional growth rate at $k=0$ gets closer to the inviscid value obtained by Carnevale and Kloosterziel⁸ (marked by a cross in Fig. 5) when the Reynolds number is increased.

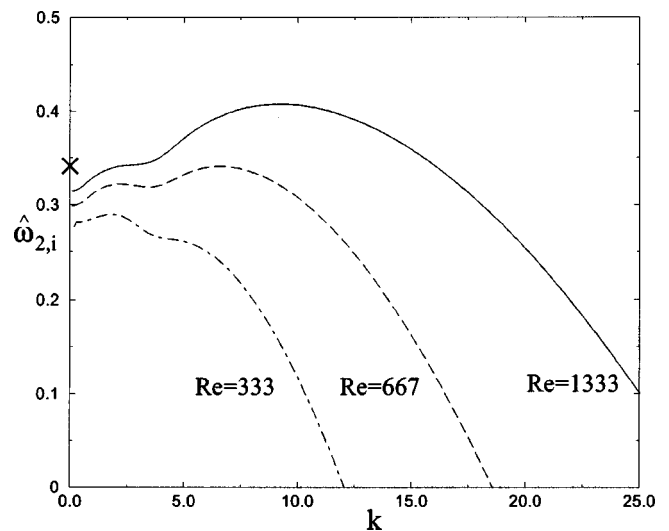


FIG. 5. Growth rate $\hat{\omega}_{2,i}$ of the $m=2$ mode as a function of k for $\alpha=5$ and different Reynolds numbers: $Re=1333$ (continuous line), $Re=667$ (dashed line), and $Re=333$ (dashed-dotted line).

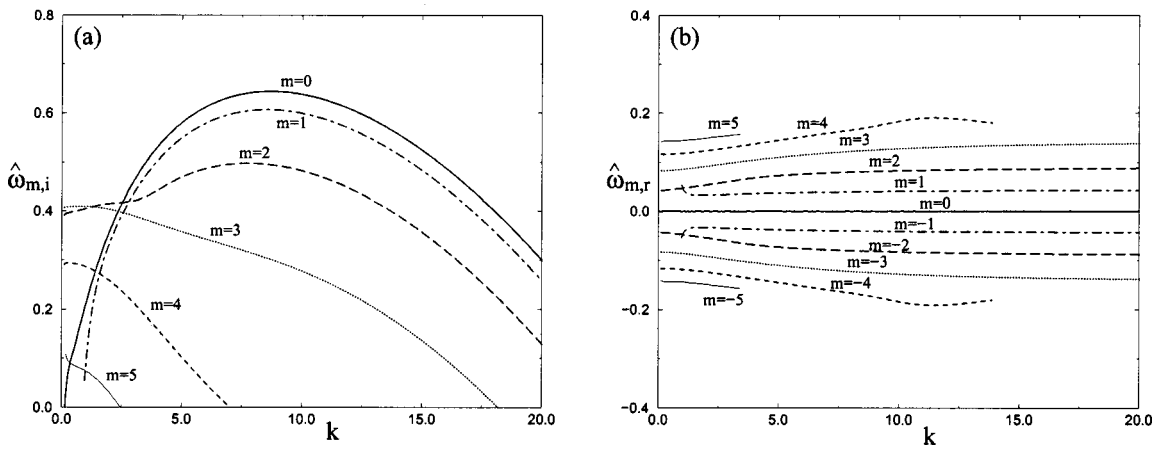


FIG. 6. Temporal growth rate (a) and angular frequency (b) as a function of the axial wavenumber k for $\alpha=7$ and various values of m .

Note that the Reynolds number based on the shear layer thickness is about 500 for $Re=1333$ (Re being based on the radius), so that it is not surprising that viscous effects are quite large on the growth rate at $k=0$. The fact that the cutoff wavenumber increases with the Reynolds number (Fig. 5) is in agreement with the ultraviolet catastrophe behavior shown by Smyth and McWilliams.¹² The centrifugal instability would destabilize high wavenumbers if the fluid were inviscid, with a growth rate approaching a constant value σ_m^∞ , when k goes to infinity. When viscous effects are taken into account, a cutoff wavenumber is introduced that scales like $\sqrt{\sigma_m^\infty Re}$. This scaling is indeed in good agreement with Fig. 5 since $(k_c^c)^2/Re$ is approximately constant, varying from 0.44 for $Re=333$ to 0.49 for $Re=667$, and to 0.54 for $Re=1333$.

Figure 6 is similar to Fig. 3 except that the steepness parameter is higher and equals $\alpha=7$. Modes $m=2, 3, 4, 5$ are now unstable at $k=0$; this illustrates the fact that the azimuthal cutoff wavenumber m_α is increasing with α . This becomes particularly clear in Fig. 7(b), which depicts the growth rate of each azimuthal mode at $k=0$, ($\hat{\omega}_{m,i}^0 \equiv \hat{\omega}_{m,i}(k=0)$) as a function of α . As the value of the steepness parameter α is increased, higher and higher azimuthal modes become unstable. This result is entirely consistent with previous studies.^{8,9} Flierl found that, the smaller the relative

width of the outer annulus of opposite vorticity, the larger the number of unstable azimuthal modes. This might be understood by drawing an analogy with plane shear layers. The cutoff wavenumber m_α is then determined by the perimeter divided by the shear thickness, which is itself inversely proportional to α , implying that m_α grows like α . Moreover, in this two-dimensional limit, the steeper the velocity profile, the higher the wavenumber of the fastest growing mode. In the 2D limit ($k=0$), stability results of Carton and McWilliams,¹ Carnevale and Kloosterziel,⁸ and Orlandi and Carnevale⁴ are confirmed when viscosity is added [Fig. 7(a)]. The increase in the steepness α is associated to an increase of the highest wave unstable at $k=0$, m_α . For α slightly above 6, the most unstable mode switches from $m=2$ to $m=3$.

When k increases, the same trends as for $\alpha=4$ (Fig. 3) are observed in Fig. 6 for $\alpha=7$. Modes $m=0$ and $m=1$, which are stable at $k=0$, are the most unstable modes, the maximum being reached at k close to $k \sim 8$, a value larger than for $\alpha=4$ [see also Figs. 7(b) and 7(c)]. The axisymmetric mode $m=0$ reaches the overall highest growth rate as for $\alpha=4$. As seen in Fig. 7, the most unstable mode continues being $m=0$, for all α tested and is closely followed by $m=1, m=2$, and so on. The maximal growth rate $\hat{\omega}_{m,i}^{\max}$ is a monotonically decreasing function of m and a monotonically increasing function of α . Mode $m=2$ presents two local

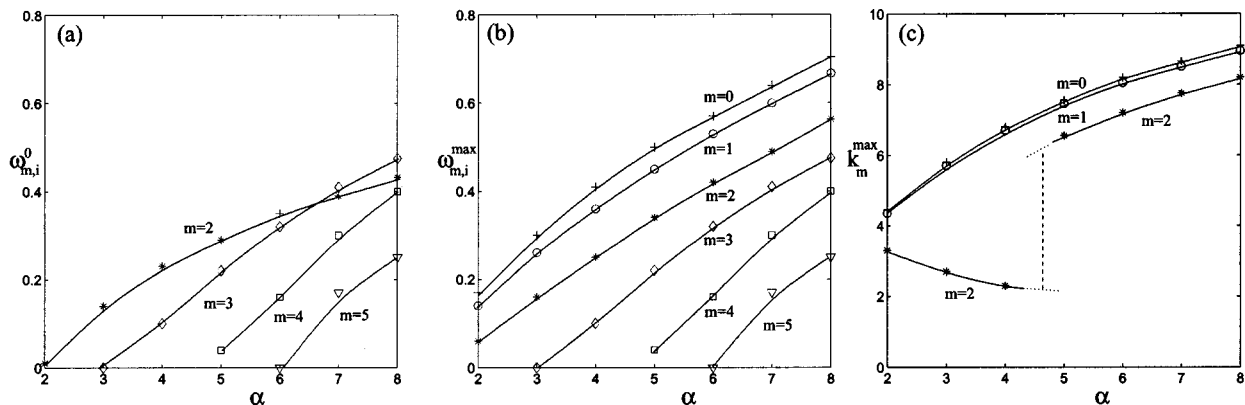


FIG. 7. Effects of the steepness parameter α . (a) Growth rate $\hat{\omega}_{m,i}^0$ at $k=0$ for $m \geq 2$; (b) maximal growth rate $\hat{\omega}_{m,i}^{\max}$ versus the steepness parameter α for various values of m ; (c) k_m^{\max} when nonzero.

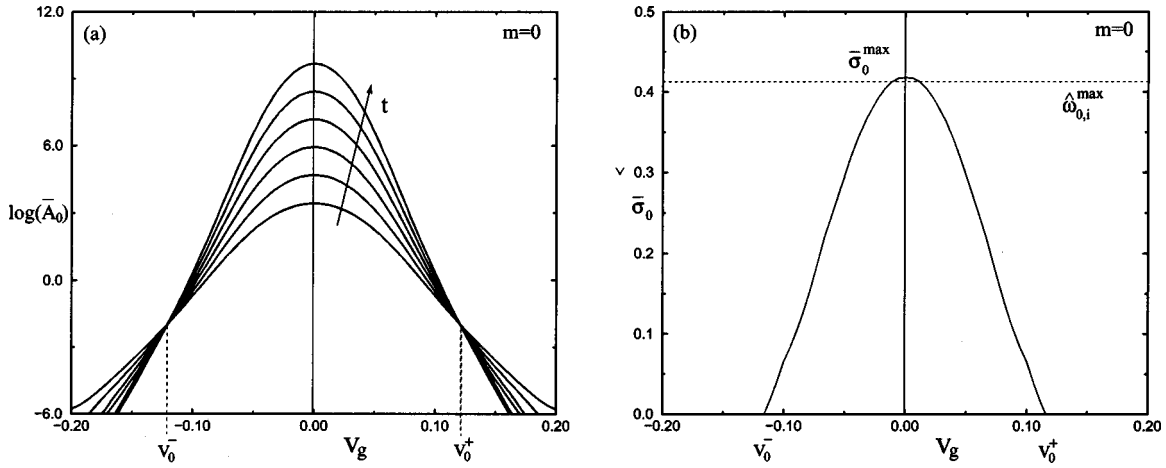


FIG. 8. (a) Demodulated amplitude $\bar{A}_0(v_g, t)$ of the $m=0$ wave-packet component with respect to group-velocity x/t on a semilog plot for $\alpha=4$ at different times from $t=15$, $t=18$, $t=21$, $t=24$, $t=27$, and $t=30$ with Hilbert transform; the trailing (respectively, leading) edge of the wave packet are denoted by v_0^- (respectively, v_0^+). (b) Associated growth rate $\bar{\sigma}_0(x/t)$. Note that the maximum spatio-temporal amplification rate $\bar{\sigma}_0^{\max}$ is nearly equal to its temporal counterpart $\hat{\omega}_{0,i}^{\max}$.

maxima in $k=2.5$ and $k=7.7$, but the global maximum is the second peak in contrast to Fig. 3(a). Accordingly, in Fig. 7(c), $k_2^{\max}(\alpha)$ presents a discontinuity in $\alpha=5$ associated with a shift of the absolute maximum from the first peak to the second peak. Modes $m=3$, $m=4$, and $m=5$, which are unstable at $k=0$, achieve their maximum growth rate precisely at $k=0$.

In conclusion, from the temporal stability point of view, the most intense instability is therefore the pure axisymmetric instability, for which the instability reduces to centrifugal instability.

V. SPATIO-TEMPORAL EVOLUTION OF THE WAVE PACKET

This section describes the spatio-temporal spreading of the wave packet generated by a localized impulse. As a typical example, Fig. 8(a) displays the demodulated amplitude of the wave packet $\bar{A}_0(v_g, t)$ corresponding to the axisymmetric mode ($m=0$) on a semilog plot as a function of the group velocity $v_g = x/t$ at different times.

It is seen that the wave packet only grows in a region $[v_0^-; v_0^+]$, where v_0^- and v_0^+ are, respectively, the group velocity of the trailing and leading edges of the $m=0$ wave packet. Note that $v_0^- = -v_0^+$ because of the symmetry property (30b). The corresponding spatio-temporal growth rate $\bar{\sigma}_0(v_g)$ evaluated through relation (19) is depicted in Fig. 8(b). More generally, the curve $\bar{\sigma}_m(v_g)$ contains all the information characterizing the spatio-temporal growth of the wave packet. Its extent is in fact delimited by the rays moving at the trailing and leading edge velocities, v_m^- and v_m^+ , along which neutral waves are observed. Formally, they might be defined by the conditions $\bar{\sigma}_m(v_m^-) = 0$ and $\bar{\sigma}_m(v_m^+) = 0$, with $v_m^- < v_m^+$. In the present case ($m=0$), only one connected region of unstable group velocities $[\bar{\sigma}_m(v_g) > 0]$ is observed and the velocities v_0^- and v_0^+ are unambiguously defined. Let v_m^{\max} denote the spatio-temporal ray along which the largest temporal growth rate $\bar{\sigma}_m^{\max}$ is observed. According to Delbende *et al.*¹⁹

$$\bar{\sigma}_m^{\max} = \hat{\omega}_{m,i}^{\max}, \quad (33)$$

i.e., the maximum temporal amplification rate coincides with its maximum spatio-temporal counterpart, which is attained for a real wavenumber k_m^{\max} . This most amplified wave propagates at the real group velocity

$$v_m^{\max} = \frac{d\hat{\omega}_{m,r}}{dk}(k_m^{\max}). \quad (34)$$

Both cross checks (33) and (34) are verified in Fig. 8(b) for $m=0$ since the maximum $\bar{\sigma}_0$ is attained in $v_0^{\max} = 0$ for $\bar{\sigma}_0^{\max} = 0.42 \pm 0.01$, a value particular close to the temporal maximal growth rate $\hat{\omega}_{0,i}^{\max} = 0.41 \pm 0.01$.

As another illustrative example, Fig. 9(a) displays the logarithm of the demodulated amplitude of the $m=+2$ and $m=-2$ modes, $\bar{A}_{+2}(v_g, t)$ and $\bar{A}_{-2}(v_g, t)$ as a function of the ray velocity $v_g = x/t$ at different times t for $\alpha=4$. In the middle of the wave packet the Hilbert transform allows us to discriminate between amplitude and phase and to properly extract the wave-packet envelope. However, in Fig. 9(a), the drawback of the application of the Hilbert transform is also seen since “tails” develop (due to the convolution with $1/x$) which prevent us from observing the edges of the wave packet and therefore from measuring their speed. Neither the trailing-edge velocities v_{-2}^- and v_{+2}^- nor the leading edge velocities v_{-2}^+ and v_{+2}^+ can be evaluated with precision. The symmetry $\bar{A}_{-2}(-v_g) = \bar{A}_{+2}(+v_g)$ [see Eq. (30a)] is verified, inducing $v_{-2}^- = -v_{+2}^+$ and $v_{-2}^+ = -v_{+2}^-$. Despite the apodization of the wave packets, it can be expected that $v_{-2}^- < v_{+2}^- < 0$ and by symmetry $0 < v_{-2}^+ < v_{+2}^+$.

In order to measure the edge velocities with accuracy, we have to resort to the wave packet amplitude defined from the initial signal without applying the demodulation with the Hilbert transform, i.e., to the amplitude $\tilde{A}_{|2|}$, as defined in (26). As explained in Sec. III, the use of $\tilde{A}_{|2|}$ hinders the separation of contributions of positive helical mode (usual convention $m=+2$) and negative helical modes (convention $m=-2$), this separation being left for a later section when

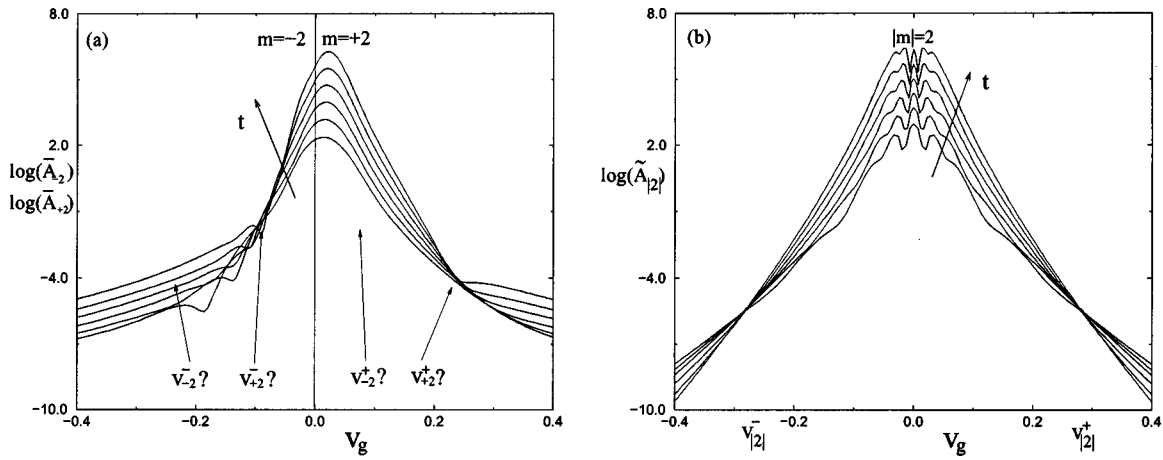


FIG. 9. Evolution in time of the wave packet for $|m|=2$. (a) Demodulated amplitudes $\bar{A}_{+2}(v_g, t)$ (continuous line) and $\bar{A}_{-2}(v_g, t)$ (dotted line) of the $m=2$ wave-packet component with respect to group-velocity x/t on a semilog plot for $\alpha=4$ at different times from $t=15, t=18, t=21, t=24, t=27$ to $t=30$. (b) Same for the amplitude $\tilde{A}_{|2|}$ (without demodulation).

the local phase will be computed and its variations followed in time. Figure 9(b) shows the amplitude $\tilde{A}_{|2|}(v_g)$ as a function of v_g for different times. The apodization suffered by the demodulated amplitude \bar{A}_2 does not hold for $\tilde{A}_{|2|}$, and $\tilde{A}_{|2|}$ reaches for instance e^{-10} at $x/t = \pm 0.4$, whereas the Hilbert transform has artificially raised the amplitude at the same group velocity in Fig. 9(a) to e^{-5} , preventing us from observing properly the edges of the wave packet. Oscillations, particularly visible in the center of the wave packet, correspond to spatial variations of the local phase since no demodulation has been applied. Despite this phase jitter, the wave packet seems localized between well-defined edges outside of which the amplitude decreases with time. The determination of the edge group velocities is subjected to phase jitter due to the absence of separation of amplitude and phase, although it is less marked than in the middle of the wave packet where the signal oscillates strongly. It must be understood that the Fourier transform oscillates in regions where both the positive and the negative helical mode are unstable and therefore “mixed.” By contrast, in regions where only one sense of winding is unstable and the other quenched, as for instance in the interval $[v_{-2}^-; v_{+2}^+]$, the Fourier transform amplitude stops oscillating and the phase jitter is negligible. Although a better determination would be achieved by a longer time integration, necessitating in turn a longer box, the accuracy in the estimation of the edge velocities $v_{|2|}^-$ and $v_{|2|}^+$ of the overall $|m|=2$ wave packet is satisfactory. The sign of the actual winding on each edge is determined according to continuity arguments. A comparison of Figs. 9(a) and 9(b) leads us to expect that $v_{|2|}^-$ might be attributed to a negative $m=-2$ helical mode and $v_{|2|}^+$ to its positive counterpart. The edge velocities v_{-2}^+ and its opposite v_{+2}^- may only be roughly estimated from the demodulated amplitudes in Fig. 9(a) suffering from apodization, since these edges are overwhelmed by the growing part of the $|m|=2$ wave packet when the two positive and negative helical modes are mixed through the Fourier transform in Fig. 9(b).

The edge velocities defined with Hilbert transforms for

the $m=0$ and $m=\pm 1$ modes and with Fourier transforms for $|m|\geq 2$ have been systematically evaluated for various α in the range $\alpha \in [2;8]$ with a precision generally better than 1% and at most 5%. Overall results are displayed in Fig. 10, which compares the spreading velocities of the different azimuthal m components as a function of the steepness parameter α . For each $+m/-m$ azimuthal wavenumber pair, only the outermost edge velocity has been reported. It is seen that the mode spreading out the fastest is $|m|=2$ in the whole range of $\alpha \in [2;8]$ presently studied. Though the most amplified mode is $m=0$ in the center of the wave packet, the edges of the wave packet are formed by helical structures with $|m|=2$, no matter how intense the azimuthal shear. Implications of this physical picture are discussed in the final section.

VI. DETAILED STUDY OF THE WAVE PACKET

It was seen in the preceding section that, except for modes $m=0$ and $|m|=1$, the evaluation of $\sigma_m(x/t)$ is diffi-

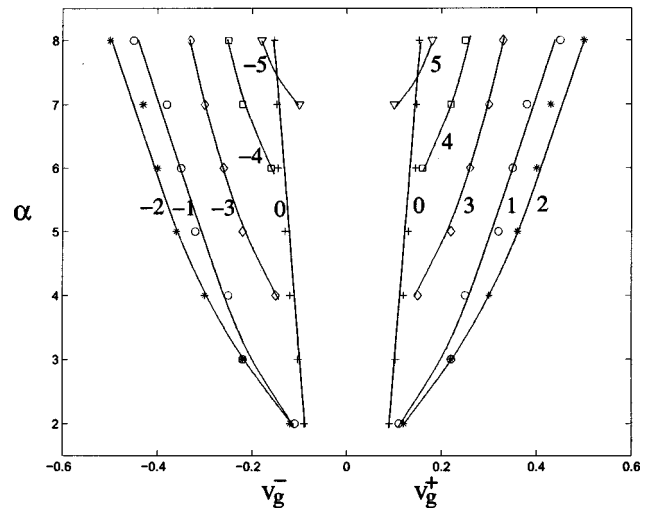


FIG. 10. Group velocities of the downstream and the upstream edges of the wave packet as a function of α for different m .

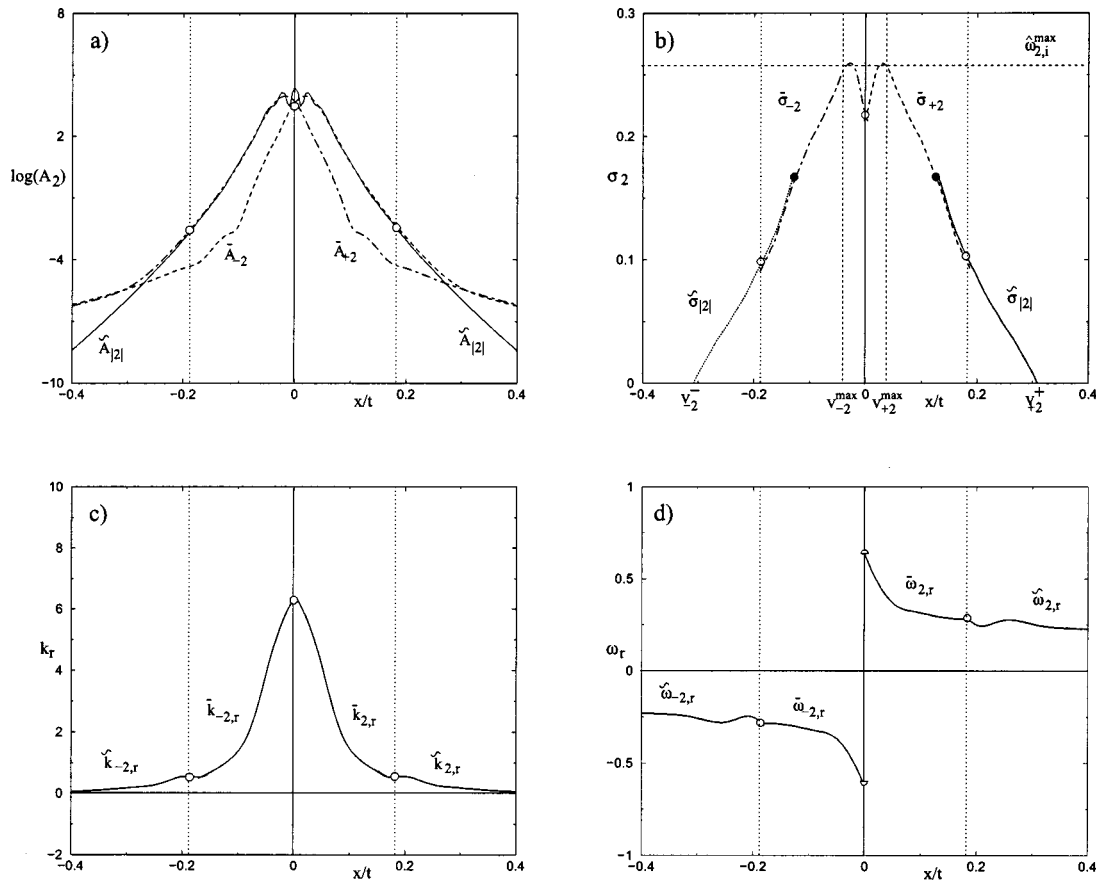


FIG. 11. Detailed study of the wave-packet $|m|=2$ component for $\alpha=4$. (a) Hilbert-transformed amplitudes \bar{A}_{+2} (dotted-dashed), \bar{A}_{-2} (dashed), and Fourier-transformed amplitude $\tilde{A}_{|2|}$ (full line) as function of $v_g = x/t$ at $t=18$. (b) Corresponding growth rates $\bar{\sigma}_{+2}$, $\bar{\sigma}_{-2}$ and $\bar{\sigma}_{|2|}$; in each flow direction, upstream and, respectively, downstream, $\bar{\sigma}_{+2}$ and $\bar{\sigma}_{-2}$ (respectively, $\bar{\sigma}_{-2}$ and $\bar{\sigma}_{|2|}$) overlap on a ray interval contained between the hollow circle (vertical dotted line) and the full circle; the horizontal and vertical dashed lines correspond, respectively, to the predicted values from temporal theory of the maximum growth rate and of its corresponding opposite group velocities. (c) and (d) Associated composite wavenumber $k_{2,r}$ and frequency $\omega_{2,r}$.

cult, since in the middle of the wave packet it should be extracted out of the Hilbert transformed amplitudes, whereas on the edges it should be extracted out of the Fourier amplitudes. Such an effort has been made in Fig. 11 for the same parameter settings as in Fig. 9.

Figure 11(a) reproduces the Hilbert- and Fourier-transformed amplitudes \bar{A}_{+2} (dotted-dashed line), \bar{A}_{-2} (dashed line), and $\tilde{A}_{|2|}$ (full line) taken from Figs. 9(a) and 9(b) at time $t=18$. Please note the apodization of the wave packet when the Hilbert transform is used. The precise cutoff value of the group velocity v_g for which the analytical signal amplitudes become irrelevant is difficult to establish on the graph at a single time. It is, however, more easily determined when the growth rate is evaluated and convergence required. Figure 11(b) depicts the growth rates calculated at $t=18$ through either Hilbert transform $\bar{\sigma}_{+2}$ and $\bar{\sigma}_{-2}$ or Fourier transform $\tilde{A}_{|2|}$. For each growth rate, the convergence criterion (described in Sec. III B) is only verified in a range of group velocities. The Hilbert-transformed growth rates converge, respectively, up- and downstream in a range between the hollow circle at $v_g = \pm 0.18$ and the hollow circle on the zero group velocity ray, whereas the Fourier-transformed growth rates converge outside the range between the two dark circles at $v_g = \pm 0.13$. There are two symmetric regions

of overlap where the two determinations coincide. A “construction rule” for the composite growth rate is then defined as follows. The wave packet is made of four parts from downstream to upstream: (a) an $m=-2$ trailing edge $\bar{\sigma}_{|2|}$; (b) the “heart” of the $m=-2$ wave packet $\bar{\sigma}_{-2}$ (when converged); (c) the “heart” of the $m=+2$ wave packet $\bar{\sigma}_{+2}$ (when converged); and (d) an $m=2$ leading edge $\bar{\sigma}_{|2|}$. The wave packet splits into two parts symmetric with respect to the $v_g=0$ axis with opposite group velocities $v_{+2}^{\max} = -v_{-2}^{\max}$ at their equal maximal growth rates and opposite edge velocities $v_{+2}^+ = -v_{-2}^-$: one part is mostly propagating in the positive direction (the $m=+2$ mode) and the other one mostly in the negative direction (the $m=-2$ mode). In Fig. 11(b), the maxima of the wave packets $m=+2$ (respectively, $m=-2$) and their corresponding group velocities v_{+2}^{\max} (respectively, v_{-2}^{\max}) obtained through temporal stability theory are depicted by dashed lines. It is seen that the cross checks of (33) and (34) are verified in a good approximation.

In Figs. 11(a) and 11(b), the edges have been labeled $m=-2$ at the trailing edge and $m=+2$ at the leading edge according to continuity arguments. To determine the spatial winding, the local wavenumber $\tilde{k}_{m,r}$ has to be computed. Figure 11(c) presents the composite local wavenumber $k_{2,r}$ corresponding to the wave packet shown in Fig. 11(b). With

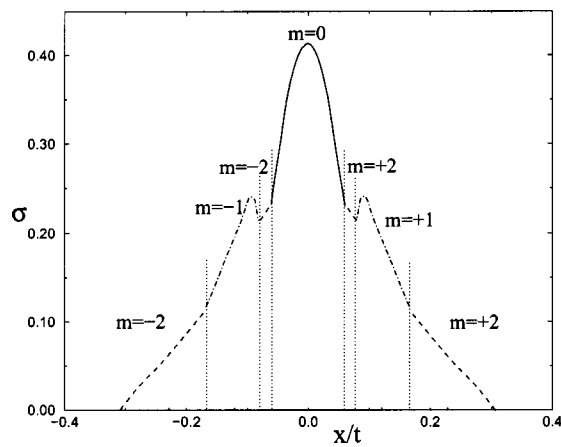


FIG. 12. Structure of the wave packet; $\sigma_m(x/t)$ for $\alpha=4$ and different m .

the preceding “construction rule” of the wave packet, one can see that $k_{2,r}$ is again composed of four parts in cascade, $\tilde{k}_{-2,r}$, $\tilde{k}_{-2,r}$, $\tilde{k}_{+2,r}$, and $\tilde{k}_{+2,r}$. Since the direction of winding is given by the sign of m in the inner parts of the wave packet when the Hilbert transform is performed (we hereby verify that $\tilde{k}_{m,r}$ is positive, as implicitly forced by the Hilbert transform) and by the sign of the product $\tilde{k}_{m,r} \times m$ in the outer parts when the Fourier transform is performed, Fig. 11(c) shows that the winding of the wave is positive for $v_g > 0$ and negative for $v_g < 0$. It follows in particular that the helix is screwed negatively at the trailing edge and positively at the leading edge. Figure 11(d) presents the composite frequency $\omega_{2,r}$, which is again the combination of four expressions respecting the same construction rule. In the downstream part of the wave packet, the frequency is negative (as well as m), whereas in the upstream part the frequency is

positive (as well as m), showing that on both edges the structure rotates in the same direction as the vortex.

The composite growth rates $\sigma_m(v_g)$ corresponding to different values of m have been computed and may be combined for $\alpha=4$ to produce the wave-packet envelope as reported in Fig. 12. The full wave packet has a stratified shape with the most unstable temporal mode $m=0$ dominating in the inner part of the wave packet. Further away from the ray with zero group velocity in the positive direction $v_g > 0$ (respectively, negative direction $v_g < 0$), the mode $m=+2$ (respectively, $m=-2$) takes over in a small ray interval, quickly followed by mode $m=+1$ (respectively, $m=-1$) possessing the largest growth rate until the edges are left to the $m=+2$ (respectively, $m=-2$) mode. We have verified that the conclusions presented in Fig. 11 for $|m|=2$ still hold for all $|m|>0$; the $v_g < 0$ part of the wave packet is made of negative helical modes rotating in time in the same direction as the vortex, whereas the $v_g > 0$ part of the wave packet is made of positive helical modes rotating in time in the same direction as the vortex. A three-dimensional representation of the wave packet can be found in Fig. 13. On the downstream boundary of the wave packet, opposite ISO-surfaces of the vorticity reveal an $m=-2$ mode with negative winding. In the middle of the wave packet, the $m=0$ mode is taking over, as evidenced by the rings in the middle of the wave packet.

VII. DISCUSSION AND CONCLUSIONS

This study aimed at understanding the instability and wavenumber selection mechanisms of an isolated vortex and the interplay of the centrifugal and azimuthal shear instabilities. From a temporal point of view, the centrifugal instability has been shown to dominate over the azimuthal shear

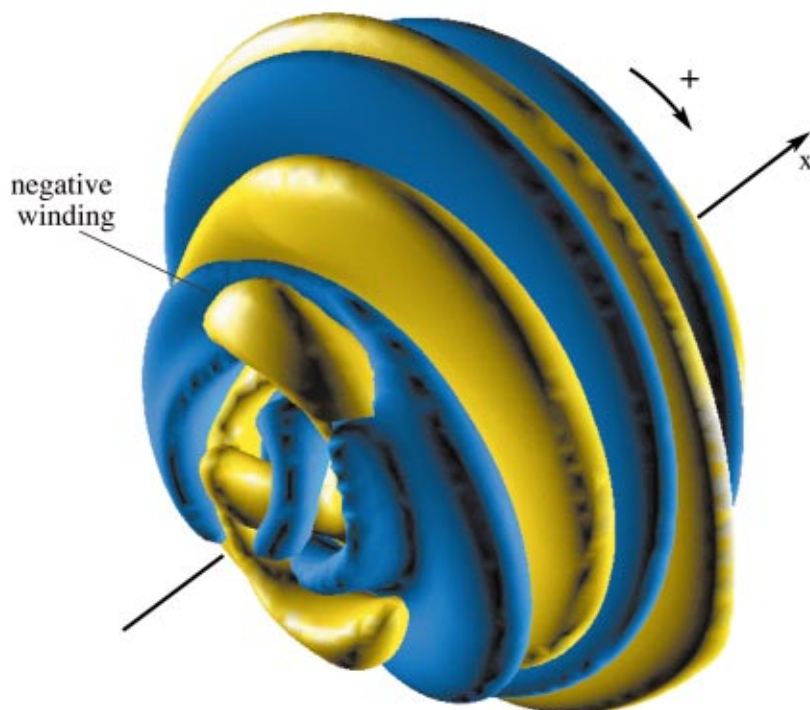


FIG. 13. (Color) ISO-surfaces of the vorticity at time $t=15$ for $\alpha=4$. In blue $\omega_x=0.5\omega_{\max}$, in yellow $\omega_x=-0.5\omega_{\max}$.

instability since the axisymmetric ($m=0$) mode, which is only sensitive to the centrifugal instability, is the most temporally amplified for all the steepness parameter considered. This result strongly supports the interpretation of Kloosterziel and van Heijst⁵ that, in the presence of background rotation, the centrifugal instability acting on anticyclones can quench the azimuthal instability and prevent the flow from developing into a tripole.

As far as the spreading of a wave packet along a columnar vortex is concerned, we have shown that the $m=+2$ mode is traveling the fastest in the positive x direction, whereas $m=-2$ is symmetrically the fastest in the $x<0$ direction. The response of an isolated vortex to a localized perturbation in space and time is therefore dominated on the edges of the perturbation by double helices twisting the vortex and propagating away from the initial location of the perturbation.

As mentioned in the Introduction, the stability of “worms” is still an open issue. Cadot *et al.*¹³ suggested that the axial jet could be responsible for their explosion through a vortex breakdown phenomenon that would most likely be an axisymmetric bursting. Eloy¹⁷ focused on the role of a strain field in sustaining the elliptic instability and predicted that a single helix is the most amplified mode. Figure 13 reveals a structure of the unstable vortex which compares favorably with flow visualizations of Cadot *et al.*¹³ They observed that worms were bursting through double-helical distortions resembling the helical $m=2$ structures propagating the fastest on our vortex. Nevertheless, it remains to be assessed if a worm could be considered as an isolated vortex. In a less turbulent flow, Bottausci and Petitjean¹⁸ have recently reported the bursting of vortices produced by sucking the boundary layer of a channel flow. Velocity measurements show that the circulation of the vortex decreases away from the core, thereby pointing to an isolated vortex. Flow visualizations moreover indicate that destabilization and transition occur through multiple helices. This behavior is consistent with the present prediction, but a more definite statement would require the analysis of more realistic profiles since in Bottausci and Petitjeans’¹⁸ experiment the decrease of the circulation is very slow away from the vortex center. An analysis is in progress, which combines isolated azimuthal and axial velocity profiles characteristic of swirling jets using the same methodology as presented here.

ACKNOWLEDGMENTS

I. Delbende is kindly acknowledged for his incomparable know-how. The authors thank P. Billant and P. Manneville for careful reading of the manuscript. The work is supported by the French Ministry of Defense under Grant No. 99 001004707588 and by IDRIS (CNRS) for computational facilities under Project No. 020174.

¹X. Carton and J. McWilliams, “Barotropic and baroclinic instabilities of axisymmetric vortices in a quasi-geostrophic model,” in *Mesoscale/Synoptic Coherent Structures in Geophysical Turbulence*, edited by J. Ni-houl and B. Jamart (Elsevier, New York, 1989), pp. 225–244.

- ²L. Rayleigh, “On the dynamics of revolving fluids,” *Proc. R. Soc. London, Ser. A* **93**, 148 (1916).
- ³E. Hopfinger and G. van Heijst, “Vortices in rotating fluids,” *Annu. Rev. Fluid Mech.* **25**, 241 (1993).
- ⁴P. Orlandi and G. Carnevale, “Evolution of isolated vortices in a rotating fluid of finite depth,” *J. Fluid Mech.* **381**, 239 (1999).
- ⁵R. Kloosterziel and G. van Heijst, “An experimental study of unstable barotropic vortices in a rotating fluid,” *J. Fluid Mech.* **223**, 1 (1991).
- ⁶R. Kloosterziel and G. van Heijst, “The evolution of stable barotropic vortices in a rotating free-surface fluid,” *J. Fluid Mech.* **239**, 607 (1992).
- ⁷G. van Heijst, R. Kloosterziel, and C. Williams, “Laboratory experiments on the tripolar vortex in a rotating fluid,” *J. Fluid Mech.* **225**, 301 (1991).
- ⁸G. Carnevale and R. Kloosterziel, “Emergence and evolution of triangular vortices,” *J. Fluid Mech.* **259**, 305 (1994).
- ⁹G. Flierl, “On the instability of geostrophic vortices,” *J. Fluid Mech.* **197**, 349 (1988).
- ¹⁰J.-M. Chomaz, M. Rabaud, C. Basdevant, and Y. Couder, “Experimental and numerical investigation of a forced circular shear layer,” *J. Fluid Mech.* **187**, 115 (1988).
- ¹¹P. Gent and J. McWilliams, “The instability of barotropic circular vortices,” *Geophys. Astrophys. Fluid Dyn.* **35**, 209 (1986).
- ¹²W. Smyth and J. McWilliams, “Instability of an axisymmetric vortex in a stably stratified, rotating environment,” *Theor. Comput. Fluid Dyn.* **11**, 305 (1998).
- ¹³O. Cadot, S. Douady, and Y. Couder, “Characterization of low-pressure filaments in a three-dimensional turbulent shear flow,” *Phys. Fluids* **7**, 630 (1995).
- ¹⁴Morris and R. Goscinny, *Lucky-Luke, a Poor Lonesome Cow-Boy* (Dupuis, Paris, 1954).
- ¹⁵P. G. Saffman, *Vortex Dynamics* (Cambridge University Press, Cambridge, UK, 1992).
- ¹⁶C.-Y. Tsai and S. Widnall, “Examination of a group-velocity criterion for breakdown of a vortex flow in a divergent duct,” *Phys. Fluids* **23**, 864 (1980).
- ¹⁷C. Eloy, “Instabilité multipolaire de tourbillons,” Ph.D. thesis, Université de la Méditerranée Aix-Marseille II (2000).
- ¹⁸F. Bottausci and P. Petitjean, “Visualizations of stretched vortices,” in *Vortex Structure and Dynamics, Lecture Notes in Physics*, edited by A. Maurel and P. Petitjean (Springer, Berlin, 1999), pp. 124–134.
- ¹⁹I. Delbende, J.-M. Chomaz, and P. Huerre, “Absolute/convective instabilities in the Batchelor vortex: A numerical study of the linear impulse response,” *J. Fluid Mech.* **355**, 229 (1998).
- ²⁰P. Huerre and M. Rossi, “Hydrodynamic instabilities in open flows,” in *Hydrodynamic and Nonlinear Instabilities*, edited by C. Godrèche and P. Manneville (Cambridge University Press, Cambridge, 1998), pp. 81–294.
- ²¹J. Flor and G. van Heijst, “Stable and unstable monopolar vortices in a stratified fluid,” *J. Fluid Mech.* **311**, 257 (1996).
- ²²P. Drazin and W. Reid, *Hydrodynamic Stability* (Cambridge University Press, Cambridge, 1981).
- ²³J. L. Synge, “The stability of heterogeneous liquids,” *Trans. R. Soc. Can.* **27**, 1 (1933).
- ²⁴S. Leibovich and K. Stewartson, “A sufficient condition for the instability of columnar vortices,” *J. Fluid Mech.* **126**, 335 (1983).
- ²⁵H. Ludwig, “Ergänzung zu der Arbeit: Stabilität der Strömung in einem zylindrischen Ringraum,” *Z. Flugwiss.* **9**, 359 (1961).
- ²⁶P. Brancher and J.-M. Chomaz, “Absolute and convective instabilities in spatially periodic shear flows,” *Phys. Rev. Lett.* **78**, 658 (1997).
- ²⁷W. Edwards, L. Tuckerman, R. Friesner, and D. Sorensen, “Krylov methods for the incompressible Navier–Stokes equations,” *J. Comput. Phys.* **110**, 82 (1994).
- ²⁸S. Julien, J.-M. Chomaz, and J.-C. Lasheras, “Three-dimensional stability of periodic arrays of counter-rotating vortices,” *Phys. Fluids* **14**, 732 (2002).
- ²⁹A. Vincent and M. Meneguzzi, “The spatial structure and statistical properties of homogeneous turbulence,” *J. Fluid Mech.* **225**, 1 (1991).
- ³⁰P. Huerre and P. A. Monkewitz, “Absolute and convective instabilities in free shear layers,” *J. Fluid Mech.* **159**, 151 (1985).
- ³¹A. Bers, “Space-time evolution of plasma instabilities-absolute and convective,” in *Handbook of Plasma Physics*, edited by M. Rosenbluth and R. Sagdeev (North-Holland, Amsterdam, 1983), pp. 451–517.